Supplementary Information

Enhanced intracellular delivery of small molecules and drugs via non-covalent ternary dispersions of single-wall carbon nanotubes

Patrick. D. Boyer, Hengameh. Shams, Stefanie. L. Baker, Mohammad. R. K. Mofrad, Mohammad. F. Islam, and Kris Noel Dahl

Supplementary Materials and Methods

BSA-SWCNT Complex Modeling

Docking: The PatchDock[1, 2]/FireDock[3, 4] webservers were used for all docking analyses. The crystal structure of the BSA molecule (PDB ID: 4F5S) was used as the receptor, while each of the SWCNT chiralities in the solution for NIR fluorescence intensity measurements was submitted individually as the ligand molecule to the PatchDock server.[1, 2] Both geometrical compatibility and interaction energies were considered to estimate the favorability of BSA-SWCNT binding modes. The first 1,000 most favorable binding modes found from PatchDock were then submitted to FireDock for further surface refinement. After the PatchDock binding modes were re-ranked, the new top 10 modes were selected by FireDock.[3, 4] It should be noted that the BSA molecule was equilibrated in a water box using molecular dynamics (MD) simulations prior to performing any docking analyses. Although the BSA backbone was not significantly displaced during equilibration, the side chains were re-adjusted causing a notable alterations on the BSA surface. We initially used 1 nm long SWCNTs that showed a strong tendency to interact with BSA *via* their tips. This seemed to be an artifact of having finite size SWCNTs and thus longer SWCNTs (~1.5 nm) were used with increased likelihood for lateral binding to BSA.

Molecular Dynamics: Only a subset of the most prominent SWCNT chiralities was selected for further MD simulations. The NAMD 2.9 molecular dynamics package[5] and CHARMM27 force field[6] were used for all simulations. . NAMD and CHARMM27 are commonly employed for modeling similar systems.[7] The carbon atoms of the SWCNT were considered as neutral Lennard-Jones particles. The BSA molecule in complex with each of the SWCNT structures was solvated using the TIP3P explicit water model in order to improve the model accuracy. Then, counter ions were included to neutralize the system and the KCl ion concentration of the system was set to 150 mM. The 2 fs time-step was used for all MD simulations, which provided a reasonable temporal resolution. Periodic boundary conditions were applied in all directions and the box size was adjusted to satisfy the minimum image convention. In the NPT ensemble, pressure and temperature were kept constant at 1 bar and 310 K using Langevin Piston and Langevin dynamics[8], respectively. The system was minimized for 50,000 steps in order to remove all bad contacts. Particle mesh Ewald (PME) was used to model the electrostatic interactions, and the SWITCH algorithm was applied for computing van der Waals (vdW) forces with 1.2 nm as the cut-off distance. This was followed by an equilibration simulation for 1 ns prior to the production run. Simulations on each BSA-SWCNT model were performed for 5 ns that was considered as the production run used for the main analyses. System coordinates along with system properties, *e.g.* temperature, energies *etc.*, were recorded every 20 ps. All energy calculations and visualization were performed using visual molecular dynamics software (VMD).[9] All simulations ran on the XSEDE supercomputing center.

Characterization of RB-BSA Interaction

To determine the association of RB with BSA, we measured changes in the fluorescence intensity of tryptophan amino acid residues within the BSA protein. Tryptophan fluorescence is highly sensitive to the polarity of the surrounding microenvironment including changes induced by ligand binding. Stock solutions of RB at 50 μM and BSA at 1 μM were prepared in ultrapure deionized water. The 1 μM BSA solution was titrated with successive additions of RB stock solution corresponding to final RB concentrations over the range of 0 – 9.4 μM. BSA fluorescence spectra were acquired at 25 °C using a Nanolog spectrofluorometer (Horiba Jobin Yvon). To minimize the excitation of other aromatic residues, sample excitation was set at 295 nm with 5 nm slit width. Emission spectra, corrected for instrument response and normalized to lamp excitation intensity, were collected using 5 nm slit width from 300 – 400 nm with 1 nm step size. The change in BSA peak fluorescence intensity at 338 nm (after background subtraction and accounting for the dilution of protein concentration during titration) was used to calculate the extent of fluorescence quenching relative to BSA fluorescence intensity in the absence of RB. The measured fluorescence intensity was also corrected for inner filter effects estimated from[10]

$$F_{corr} = F_{obs} \cdot 10^{(A_{ex} + A_{em})/2}$$

where A_{ex} and A_{em} are the changes in absorbance caused by additional RB leading to attenuation of incident light at 295 nm and emitted light and 338 nm.

Analysis of the quenching data using the Stern-Volmer equation showed a bimolecular quenching constant two orders of magnitude above typical diffusion-controlled collision quenching values ($8.6 \times 10^{12} > 2.0 \times 10^{10}$ $M^{-1}s^{-1}$), indicating the presence of additional binding interactions.[10] To model the binding between RB and BSA, we considered RB molecules to bind independently to a set of *n* equivalent sites on BSA. Assuming a completely complexed protein is non-fluorescent, equilibrium binding parameters can be estimated from[11]

$$log\frac{F_0 - F}{F} = logK_a + n\ log[Q]$$

where F_0 and F are the fluorescence intensities in the absence and presence of quencher molecules, respectively; K_a is the association constant, n is the number of binding sites, and [Q] is the concentration of quencher molecules. A linear fit of quenched BSA fluorescence *versus* RB concentration resulted in binding affinity from the intercept and stoichiometry from the slope.

SWCNT Purification and Length Fractionation

Unpurified high pressure carbon monoxide conversion synthesis (HiPCO) SWCNTs (Unidym, Inc.) with diameters of 1 ± 0.3 nm and polydisperse lengths were purified to remove amorphous carbon and metal impurities according to previously described methods.[12, 13] Thermogravimetric analysis and wide-angle X-ray scattering confirmed that the purified sample contained < 5 wt% carbonaceous impurities and ~0.3wt% metallic impurities, with the rest of the sample being unaltered SWCNTs.[12, 13]

Purified SWCNTs were dispersed in water using sodium deoxycholate (DOC) and centrifuged at 21,000× *g* for 2 h to remove remaining SWCNT bundles according to previous methods.[14, 15] Individualized SWCNTs were length fractionated using density gradient ultracentrifugation.[16] SWCNTs in the 10^{th}-12^{th} fractions with lengths of 145 ± 17 nm were collected[17] and subsequently pelleted and burned at 300°C in wet air in the presence of H_2O_2 to remove DOC and then washed in water several times.

SWCNT Ternary Complex Dispersion and Molecular Loading

We describe the procedure in detail for complexation with RB in this section. The methods for complexation with DM were similar except where noted. RB was dissolved in ultrapure deionized water (resistivity 18.3 MΩ·cm, total oxidizable carbon < 5 ppb) at 600 μM. BSA (Sigma-Aldrich) was dissolved separately also in ultrapure deionized water at 300 μM. Equal volumes of RB and BSA solutions were mixed to achieve a final solution of 1 wt% BSA and a 2:1 molar ratio of RB:BSA. The BSA-RB mixture was incubated overnight at 4°C in the dark to promote full infiltration of RB into BSA hydrophobic cavities.

SWCNTs were non-covalently dispersed in BSA-RB using methods described previously for BSA.[18-21] Briefly, the starting SWCNT concentration was set at 0.1 wt% to provide a 10:1 protein:SWCNT weight ratio. The mixture of BSA-RB and SWCNTs were dispersed in water using a probe tip sonicator (Fisher Scientific, Sonic Dismembrator Model 100; 3 mm tip diameter) at 6 W for 2 h. Under these conditions, the ~145 nm SWCNTs were not shortened from sonication induced scission,[22] and the protein structure of BSA was altered by less than 5% (longer sonication times can lead to loss of secondary structure of the protein).[20] Suspensions were centrifuged at 21,000× *g* for 7 min (Beckman Coulter Allegra 25R Centrifuge with a TA-15-1.5 rotor) to separate individual SWCNTs which remained in the supernatant from bundles contained in the pellet. To further separate bound SWCNTs-BSA-RB complexes from free RB and BSA-RB, the supernatant was diluted in ultrapure deionized water and ultracentrifuged at 60,000 rpm (308,450× *g* max) for 2 h (Beckman Coulter Optima L-100K Ultracentrifuge with a Type 90Ti rotor) to sediment SWCNTs-BSA-RB complexes. The supernatant containing free RB and BSA-RB was discarded. The sediment containing SWCNTs-BSA-RB complexes was washed 3 times with ultrapure deionized water and resuspended at the initial concentration in only deionized water using probe tip sonication at 6 W for 30 min. Afterwards, any residual bundles were separated from individual SWCNTs through centrifugation of the suspension at 21,000× *g* for 7 min. The supernatant was collected and used immediately for cell experiments without sterilization to prevent photobleaching.

SWCNT Ternary Complex Dispersion Characterization

UV-vis-NIR absorbance spectroscopy: To quantitatively determine SWCNT concentration and qualitatively assess dispersion quality, SWCNT dispersions were examined using UV-vis-NIR absorbance spectroscopy (Varian Cary 5000 UV-vis-NIR spectrophotometer). Concentration was determined using an extinction coefficient of 2.6 (absorbance·mL)/(mg·mm) at 930 nm.[16] The sharpness and intensity of the van Hove peaks qualitatively indicate dispersion quality.[23]

Raman spectroscopy: SWCNT structure after dispersion was characterized with Raman spectroscopy. Samples diluted to 0.3 absorbance/cm in water were analyzed on an inverted, inVia confocal Raman microscope (Renishaw) using a 50× air objective with 0.75 numerical aperture (NA) and a 785 nm laser (100 mW). Spectra were acquired between 100 – 3200 cm^{-1}. The data

were normalized by the G-band intensity. The D-band-to-G-band intensity ratio (I_D:I_G) was calculated by dividing the D-band intensity at ~1300 cm^{-1} by the G-band intensity.

NIR fluorescence spectroscopy: SWCNT dispersion quality was characterized with NIR fluorescence spectroscopy (Horiba Jobin Yvon Nanolog spectrofluorometer). SWCNT samples were diluted to 0.3 absorbance/cm in water and NIR fluorescence spectra were collected with a 60 s integration time with excitation and emission slit widths of 10 nm using a liquid nitrogen cooled detector (Symphony InGaAs-1700). The excitation grating was 1200 grooves/mm and blazed at 500 nm and the emission grating was 150 grooves/mm and blazed at 1200 nm. NIR fluorescence heatmaps of instrument corrected fluorescence intensity normalized to excitation intensity were constructed using FluorEscence and Nanosizer software (Horiba Jobin Yvon) with chirality peak fits generated using a Voight 2D model. SWCNT quantum yield (QY) was determined at 2 different wavelengths corresponding to different major chiralities in the sample. The total corrected SWCNT NIR fluorescence signal per absorbance was normalized to fluorescence per absorbance of NIR dye indocyanine green with known quantum efficiency with the same system parameters.

Quantification of Loaded Molecules

To determine the loading of RB or DM on SWCNTs, ultracentrifuged, washed, and re-dispersed SWCNTs-BSA-RB or SWCNTs-BSA-DM were subjected to UV-vis-NIR absorbance spectroscopy. The peak absorbance of RB at ~567 nm or DM at ~483 nm above SWCNTs-BSA baseline absorbance at the corresponding wavelength was used to determine the concentration of RB or DM in the sample using a standard curve relating BSA-RB or BSA-DM absorbance and concentration. Note that peak absorbance of RB in SWCNTs-BSA-RB complexes was red shifted ~12 nm from typical peak absorbance of free RB or BSA-RB at ~555 nm. A similar ~10-20 nm red shift of DM with SWCNTs-BSA-DM complexes was observed, but DM absorbance was weak and broad with interference from SWCNT contributing additional uncertainty to the peak height and location.

Stimulated *In Vitro* RB Release

RB fluorescence spectroscopy measurements were performed on a Horiba Jobin Yvon Nanolog spectrofluorometer. Sample excitation was fixed at 550 nm with a 2 nm slit width. Emission spectra were collected from 555 – 615 nm with 1 nm step size and 2 nm slit width. Both excitation and emission gratings were 1200 grooves/mm blazed at 500 nm. For quantification of fluorescence changes, the maximum instrument corrected fluorescence intensity at ~575 nm normalized to the excitation intensity was used. All fluorescence measurements were normalized by the absorbance of the sample at 550 nm using a Varian Cary 5000 UV-vis-NIR spectrophotometer.

Temperature: SWCNTs-BSA-RB was diluted to 11.6 μg/mL (containing 2 μM loaded RB concentration) in ultrapure deionized water. Fluorescence and absorbance measurements of SWCNTs-BSA-RB complexes and unbound BSA-RB or RB at 2 μM were taken from 10 – 85°C in 5°C intervals. Measurements were also made at 37 °C and the denaturation temperature of native BSA, ~68°C. Temperature was controlled using FluorEscence software with a thermoelectric temperature controller (Wavelength Electronics). Measurements were made 5 min after each new temperature set point was reached to allow sufficient time for samples to reach equilibrium. Temperature controller response time between set point changes was quick, so that the total amount of time between measurements remained consistent throughout the duration of the experiment at ~5 min.

Trypsin: 1.35 mL of 11.6 μg/mL SWCNTs-BSA-RB was equilibrated at 37 °C and then diluted with 0.15 mL of 37 °C equilibrated 2.5% (w/v) trypsin in Hank's Balanced Salt Solution (HBSS) without phenol red (Corning). The sample was pipetted up and down 5 times to ensure a well-mixed solution with a new effective 1.8 μM RB concentration. Fluorescence and absorbance measurements of SWCNTs-BSA-RB complexes and unbound BSA-RB or RB at equivalent concentrations were taken immediately after mixing up to 2 h with initial measurements every 30 s. Similar measurements were repeated with ultrapure deionized water instead of trypsin at 37°C and 80°C.

Cell Culture and Treatment

J774A.1 mouse macrophage cells (ATCC TIB-67) were cultured in Dulbecco's Modified Eagle's Medium (DMEM; 4500 mg/L glucose, 4.0 mM L-glutamine, without sodium pyruvate; Thermo Scientific Hyclone), supplemented with 10% v/v fetal bovine serum (FBS; Life Technologies) and 1% v/v penicillin-streptomycin (Life Technologies). HeLa cells (ATCC CCL-2) were cultured in DMEM (1000 mg/L glucose, 4.0 mM L-glutamine, with 110 mg/L sodium pyruvate; Thermo Scientific Hyclone), supplemented with 10% v/v FBS and 1% v/v penicillin-streptomycin. Cells were maintained at 37°C and 5% CO_2.

Quantification of RB Delivery to Cells

J774A.1 cells were seeded at 1×10^4 cells/cm^2, and HeLa cells were seeded at 3×10^4 cells/cm^2 onto sterilized #1.5 coverslips and maintained in culture for 24 h. Subsequently, cells were exposed to SWCNTs-BSA-RB diluted in fresh media at concentrations of

1 and 10 μg/mL for 48 h. Side by side control exposures were performed similarly with RB and RB-BSA (2:1 molar ratio) at concentrations equal to the determined loaded RB concentration for SWCNTs, as well as 1 wt% BSA and no treatment. After 48 h, the media containing treatments was removed. Cells were washed 6 times in phosphate buffered saline (PBS) and fixed with 3.7% v/v formaldehyde (Sigma-Aldrich) for 15 min in the dark and mounted onto glass slides. Cells were imaged in phase contrast, brightfield, and fluorescence on a Leica DMI 6000B inverted light and fluorescence microscope using a 0.6 NA air condenser and a 40× (0.75 NA) oil immersion objective. For each condition, ≥ 5 fields of view with an average total ≥ 800 cells for J774A.1 and ≥ 450 cells for HeLa were analyzed. As cells were mostly confluent, the average RB fluorescence intensity per pixel per field of view was quantified in ImageJ and normalized to the number of cells for that particular field of view. The average RB intensity per cell for each treatment condition was normalized to the average intensity per cell for untreated samples.

SWCNT NIR Fluorescence Imaging

Phase contrast imaging and widefield NIR fluorescence imaging were performed on an inverted, Leica DMI 4000 light and fluorescence microscope using a 0.9 NA air condenser and a 100× (1.4 NA) oil immersion objective. A 785 nm laser (120 mW, CrystaLaser) was circularly polarized, decohered, and expanded (Thorlabs) to fill the objective back focal plane and a 320 pixel × 256 pixel liquid nitrogen cooled 2D InGaAs camera (2D-OMA V, Princeton Instruments) were interfaced with the microscope *via* a custom setup to obtain widefield NIR fluorescence images.[24] To maximize detection of SWCNT NIR fluorescence, a custom NIR filter cube (Semrock) was used within the microscope and a 900 nm long-pass filter (Thorlabs) was placed in the emission path before the detector. Control of imaging parameters and processing were performed using WinView software (Princeton Instruments). NIR fluorescence imaging experiments were performed with a laser power density of 0.06 kW/cm^2 at the sample. NIR fluorescence intensity between 900 – 1700 nm was collected after dark current background correction for integration times ≥ 20 s. Spatial maps of SWCNT NIR fluorescence intensity above noise (~50 counts/s) were performed in WinView software. NIR fluorescence images were overlaid with visible fluorescence images taken on the same microscope system for RB and DM.

Fluorescence Lifetime Imaging and Analysis

FLIM was performed as previously reported by our group[25, 26] on a Leica TCS SP5 inverted laser scanning confocal microscope using a 100× (1.4 NA) oil immersion objective. A tunable mode-locked Ti:sapphire 80 MHz pulsed laser (Chameleon, Coherent) served at the multiphoton excitation source. For RB, the multiphoton laser was tuned to 850 nm, and wavelengths of 516 – 724 nm were passed to a photomultiplier tube to detect the full range of RB emission. Time-correlated single photon counting (TCSPC) was performed using a Becker & Hickl SPC-830 counting board and controlled with SPCM software (Becker & Hickl). To enable an accurate determination of exponential decays and to minimize the coefficient of variation, 256 pixel × 256 pixel lifetime images were acquired at a scan rate of 400 Hz for at least 180 s with 220 time channels and a measurement window of 10.8 ns.[27, 28] SPCImage software (Becker & Hickl) was used to calculate the lifetime fits per pixel and render spatial lifetime images using binning, as necessary, to achieve peak photon counts of ≥ 1,000.[28, 29]

The calculated single (τ_1) and double exponential (τ_1 and τ_2) decay lifetimes, along with their relative magnitudes and corresponding goodness of fits (χ^2), were analyzed in MATLAB.[25] For double exponential decays, the mean fluorescence (τ_m) lifetime was used to represent the data, which is the weighted average of τ_1 and τ_2. FLIM images were photon peak intensity thresholded in SPCImage (Becker & Hickl) to exclude background pixels from analysis. All reported values of lifetime are the average value of τ_m averaged across n = 5 analyzed images per experimental condition. Note that each included (*i.e.*, non-thresholded) pixel represents a unique data point of τ_m. The total number of data points was > 50,000 for each experimental condition.

Quantification of Anti-Proliferative Effects from DM Delivery

HeLa cells were seeded at 3×10^4 cells/cm^2 onto sterilized #1.5 coverslips and maintained in culture for 24 h. Subsequently, cells were exposed to SWCNTs-BSA-DM diluted in fresh media at a concentration of 1 μg/mL for 48 h. Side by side control exposures were performed similarly with DM and DM-BSA (2:1 molar ratio) at concentrations equal to the determined loaded DM concentration for SWCNTs, as well as 1 wt% BSA and no treatment. After 48 h, the media containing treatments was removed. Cells were washed 3 times in PBS and fixed with 3.7% v/v formaldehyde for 15 min in the dark and mounted onto glass slides. Cells were imaged in phase contrast and fluorescence on a Leica DMI 6000B inverted light and fluorescence microscope using a 0.6 NA air condenser and a 40× (0.75 NA) oil immersion objective. For each condition, ≥ 10 fields of view with an average total ≥ 400 cells were analyzed. Proliferation was determined as a percentage of cells normalized to control cell count.

Statistical analysis

Statistical analysis was performed using a Student's *t*-test for comparisons between two samples and one-way analysis of variance (ANOVA), followed by Tukey's test, for comparison of multiple samples. Differences were considered significant if $p < 0.05$.

Supplementary Results and Discussion

BSA-SWCNT Binding Energies

We clustered similar BSA-SWCNT binding modes into more distinct modes based on spatial adjacency and selected a representative mode from each cluster for analysis (Supplementary Table 1). The interaction energies between BSA and SWCNT for all different binding modes are summarized in Supplementary Table 2. The most favorable mode is characterized by having the lowest interaction energy and is shown in bold.

Structurally, albumin is composed of 3 homologous domains (named I, II, and III) with each domain containing two separate helical subdomains (named A and B). The folded protein forms an asymmetric heart shaped structure with a cleft-like region between domains IB and IIIB. We further compared the BSA inter-domain interaction energies in the presence and absence of SWCNT. The interaction energy of a salt bridge formed by D107 and K465 at the cleft-like region enclosed by domains IB and IIIB ranged between 0 and -100 kcal/mol even in the absence of SWCNT indicating that the cleft was flexible and transitioned between closed to open states a couple times. The (9,4) SWCNT promoted this interaction for 3 ns, but eventually it was disrupted (average energy = -48 kcal/mol). Another salt bridge between E516 and K114 linking two adjacent domains IA and IIIA showed an even less stable behavior (average energy = -32 kcal/mol). We suggest that the flexibility of both size and shape of the cleft contributed to observing similar binding modes for all SWCNTs since they allowed for necessary surface adjustments with rigid SWCNTs. Moreover, there are other binding modes occurring within the same cleft that are rotated relative to the best modes but are not as favorable (Fig. S1).

Characterization of SWCNT Dispersions

We characterized the SWCNTs-BSA-RB ternary complex dispersion using characteristic Raman spectral features of SWCNTs including the G-band at ~1590 cm^{-1} resulting from sp^2-hybridized carbon, the D-band at ~1300 cm^{-1} from sp^3-hybridized carbon, and radial breathing modes (RBMs) at 200-275 cm^{-1} (Fig. S3B).[30] The intensity ratio between the D-band and G-band was < 0.04 and similar to SWCNTs-BSA and starting SWCNT power which confirmed that the dispersion process maintained SWCNT structure. Both SWCNTs-BSA-RB and SWCNTs-BSA had minimal RBM intensity > 250 cm^{-1}, which corresponds to SWCNT bundles for the 1.58 eV (785 nm) laser line used. [31] Furthermore, we observed unfiltered real-space NIR fluorescence at ~2300 cm^{-1} in the Raman spectra confirming the presence of individually dispersed SWCNTs.

To assess dispersion quality and electronic interactions within the ternary complex, we performed NIR fluorescence spectroscopy on SWCNT dispersions. Individually dispersed semiconducting SWCNTs emit NIR fluorescence at distinct wavelengths corresponding to the band gap energies of different SWCNT chiralities,[32] whereas bundles containing metallic SWCNTs quench fluorescence.[23] We found that SWCNTs-BSA-RB contained individually dispersed SWCNTs similar to SWCNTs-BSA as evidenced by NIR fluorescence from multiple different chiralities shown in a fluorescence intensity heat map over excitation and emission wavelengths (Fig. S3C and D). The distribution of chiralities was similar for SWCNTs-BSA-RB with < 1% difference in relative abundance of each chirality, except for (9,4) which was reduced by 3%, relative to SWCNTs-BSA. Compared to BSA protein alone, the interaction of BSA-RB contributed an additional red shift of ~4.7 meV and ~3.1 meV to average SWCNT excitation and emission maxima, respectively, determined from peak fits of fluorescence intensity. The quantum yield (QY) of SWCNTs-BSA-RB was determined to be ~0.011%, which was ~1.3 times less than the QY of ~0.015% for SWCNTs-BSA, despite having nearly identical absorbance and Raman dispersion characteristics.

Here, we observed BSA-RB complexes load RB molecules onto SWCNTs in what appears to be the primary mechanism of SWCNTs-BSA-RB complex formation. We also observed electronic interactions between RB and SWCNTs suggesting some RB might have adsorbed directly onto the SWCNT surface *via* π-π stacking, which added to the loaded concentration. We note that RB has been observed to directly disperse SWCNTs at favorable efficiencies compared to other fluorophores.[33] However, we found that RB alone did not disperse SWCNTs at the same concentration used for BSA-RB dispersions. RB absorbance was peak shifted from ~555 nm, alone or with BSA, to ~567 nm when complexed with SWCNTs. Further, RB fluorescence was reduced, but not peak shifted, suggesting some form of contact or static quenching *via* the formation of a non-fluorescent ground state complex.[34] Additionally, SWCNTs-BSA-RB NIR absorbance peaks were red shifted ~3 nm and broadened 2-3 nm in width compared to SWCNTs-BSA. We also observed SWCNTs-BSA-RB QY was ~1.3 times less than SWCNTs-BSA. Similar drops in QY despite good dispersion quality have been reported for adsorption of other aromatic compounds including doxorubicin and pyrenes which perturbed the electronic structure of SWCNTs through π-π stacking resulting in reduced exciton lifetimes leading to fluorescence quenching and broadening of optical transitions.[35] Despite the additional contributions of RB, we saw almost no difference in the relative abundance of different dispersed chiralities between SWCNTs-BSA-RB and SWCNTs-BSA suggesting BSA still maintains the primary role of dispersant.

Disruption of BSA *In Vitro* Triggers Release of RB from Ternary Complex

We exposed SWCNTs-BSA-RB to increasing temperature from 12°C to 85°C and calculated the change in RB fluorescence relative to the starting intensity at 12°C (Fig. 2B). The quantum efficiency of RB is temperature dependent,[36] so we used the fluorescence change of RB by itself in solution at the same starting intensity as the baseline for calculations. SWCNTs-BSA-RB fluorescence intensity increased by 57% over the temperature range. We observed only 3% fluorescence intensity increase from BSA-RB complexes without SWCNTs over the same temperature range indicating that separation from SWCNTs is the main driving force behind the increased fluorescence.

Fluorescence intensity increased rapidly after addition of trypsin before reaching a plateau of 46% increase (Fig. 2C). Similar experiments with BSA-RB complexes without SWCNTs showed a slower increase in fluorescence to a maximum 6% increase. We compared this enzyme specific release to non-specific release over the same times at 37°C with ultrapure deionized water added instead of trypsin. We observed a kinetically slower process with 14% increased fluorescence intensity for SWCNTs-BSA-RB and a slight 1% decrease in fluorescence intensity for BSA-RB complexes only.

At room temperature, the SWCNTs-BSA-RB ternary dispersion complex showed non-zero RB fluorescence intensity, which was ~18% of the maximum fluoresce intensity from a completely decomplexed system (i.e., an equivalent concentration of RB added to a solution of SWCNTs-BSA). This indicated that a fraction of RB molecules or BSA-RB complexes may have initially been free in solution or adsorbed to SWCNTs in orientations that exclude RB molecules from energy or electron transfer with SWCNTs. At 37°C steady state fluorescence measurements showed ~27% of the maximum intensity of the completely decomplexed system, suggesting that at least 2/3 of loaded RB molecules are still available for specific or long-term release in cells. Further, the decomplexation of RB from SWCNTs-BSA-RB was found to be highly sensitive to changes in temperature around 37°C. This heightened sensitivity could allow the strong NIR absorption and high thermal conductivity of SWCNTs to be used locally to trigger SWCNT heating and disruption of BSA promoting increased intracellular release to specific cells.

Supplementary Tables

Supplementary Table 1. Clustering of the binding modes

SWCNT (n,m)	Clusters of Modes	Representative Mode
Equilibrated Protein and SWCNT		
7.6	1,4, (2,3,5), (6,7,10), 8	1,5, 6, 8
8.6	1, (2,8), 3, (4,5), 6, (7,10), 9	1, 8, 3, 4, 6, 10, 9
9.4	1,2,(3,5), 4, 6, (7,9,10), 8	1, 2, 5, 4, 9, 6, 8
10.2	1, (2,6,9), (3,4), 5, 7, 8, 10	1, 6, 3, 5, 7, 8, 10

Supplementary Table 2. SWCNT interactions with equilibrated BSA

SWCNT	Binding Mode	Energy of Interaction with BSA (kcal/mol)	Hydrophobic Residue involved in the interaction*
SWCNT(7,6)	**1**	**-129.5**	**PRO110, ALA361**
	5	-88.1	PRO113
	6	-88.2	PRO35, LEU112, PRO113, PRO467, VAL468, VAL497
	8**	493.1	Penetrated
SWCNT(8,6)	1	-110.8	ALA170, ALA175, PRO179, LEU397
	3**	3305.0	Penetration
	4	-85.1	PRO113, LEU115
	6	**-120.2**	**PRO110, ALA361, PRO467**
	8	-79.6	LEU112, PRO113, LEU115, VAL468, VAL497
	9**	4468.5	Penetrated
	10	-79.1	PRO96, LEU103, ILE202
SWCNT(9,4)	1	-69.8	ALA170, ALA175, PRO179, LEU397
	2	-58.3	ALA175, LEU178, PRO179, PRO440, PRO516
	4	-84.1	PHE394, PRO440, VAL551, ALA552, ALA559
	5	-89.6	PRO35, LEU112, VAL468, VAL497
	6	**-105.6**	**ALA361**
	8	-71.3	PRO113, LEU115
SWCNT(10,2)	**1**	**-108.2**	**PRO110, ALA361**
	3	-54.6	PRO113, LEU115
	5	-37.1	VAL228
	6	-51.9	PRO467
	7	-55.7	PRO35, LEU112, PRO113, LEU115
	8	-95.0	PRO113, LEU115, PRO420, PRO467, VAL468, VAL497
	10	-97.1	PRO96, PHE227, VAL228, ALA321, ALA324

Supplementary Figures

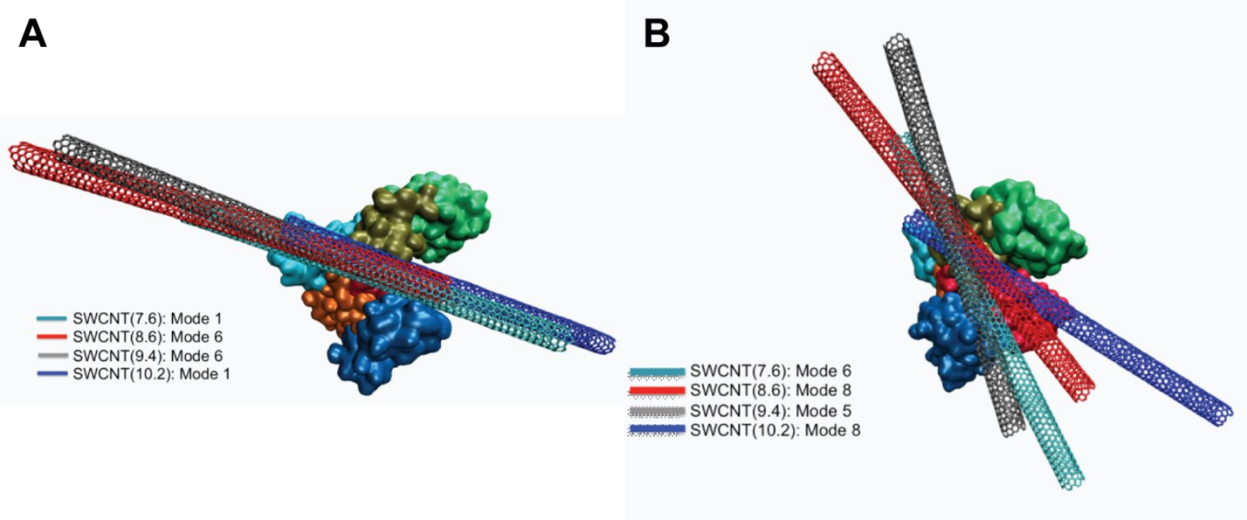

SWCNT	BSA-SWCNT Binding Energy of the Modes shown in A (kcal/mol)		BSA-SWCNT Binding Energy of the Modes shown in B (kcal/mol)	
7,6	Mode 1	-129.5	Mode 6	-88.2
8,6	Mode 6	-120.2	Mode 8	-79.6
9,4	Mode 6	-105.6	Mode 5	-89.6
10,2	Mode 1	-108.2	Mode 8	-95.0

Fig. S1. **Complex formation between BSA and SWCNTs.** (A) The lowest interaction energy binding modes from molecular docking simulations for 4 different SWCNT chiralities show a similar preference for association with BSA in the cleft-like region formed between subdomains IB (red) and IIIB (light green). (B) SWCNT binding occurs at many different orientations within the BSA cleft with slightly less favorable interaction energies indicating flexibility in the BSA cleft for accommodating rigid SWCNTs. All energies are shown in the table.

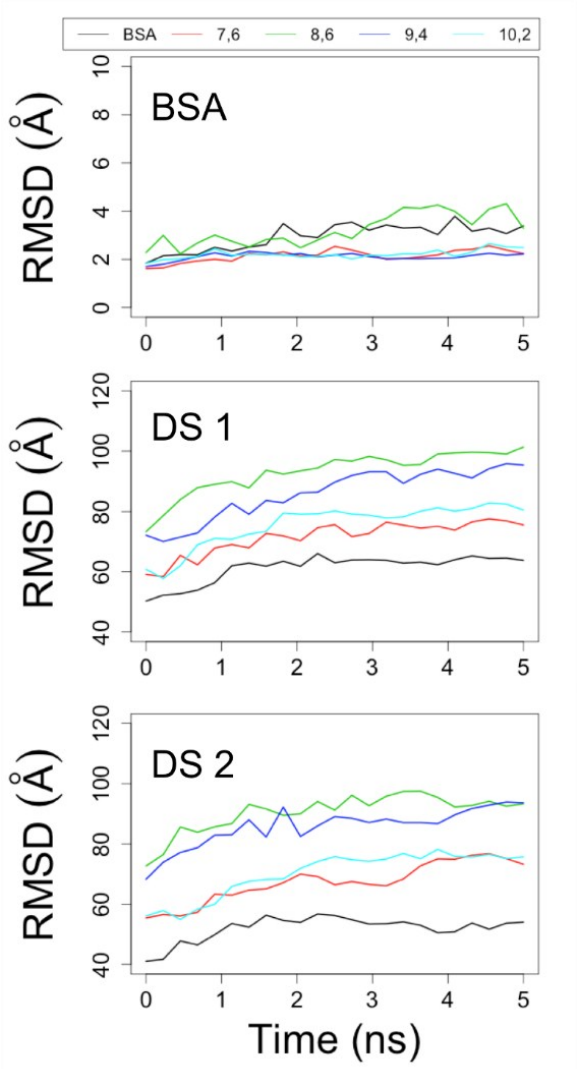

Fig. S2. **Fluctuations of the BSA protein in contact with SWCNT.** Well-docked structures of BSA are simulated over time to determine the amount of fluctuation of the protein. The root mean squared displacement (RMSD) of the protein represents the fluctuation in water. BSA tended to show less fluctuation in the presence of SWCNTs except for (8,6) SWCNT. However, both DS1 and DS2 showed higher fluctuations when BSA was bound to SWCNTs that seemed to be chirality-dependent. Note the scale difference between BSA and drug site RMSD plots.

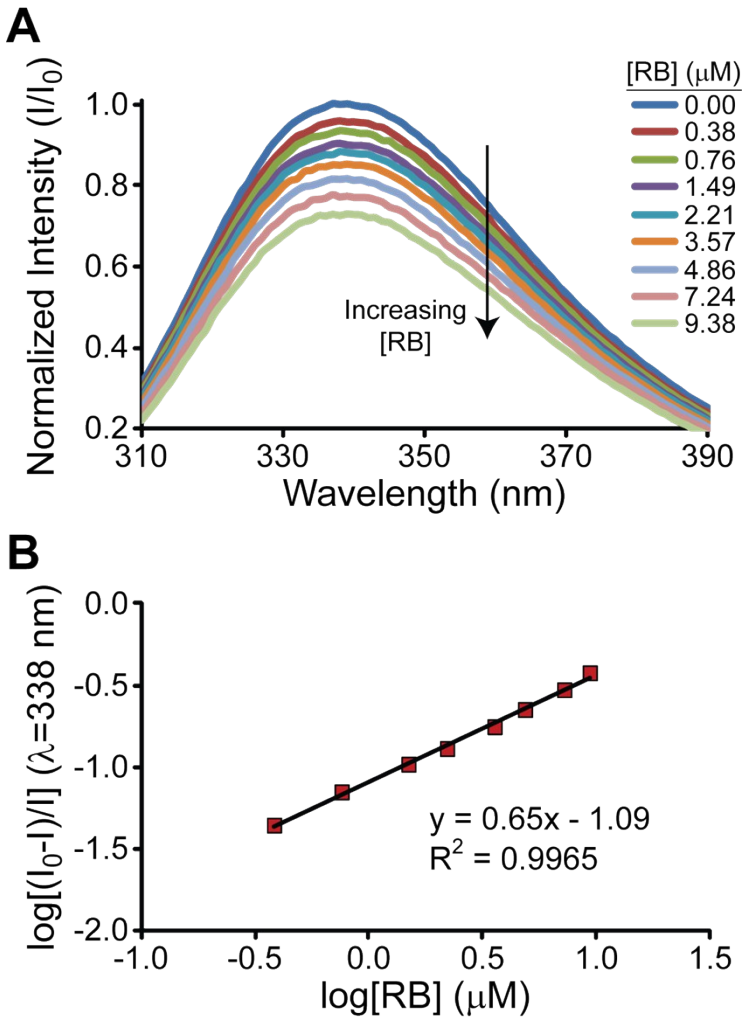

Fig. S3. Characterization of RB-BSA interactions with fluorescence spectroscopy. (A) The fluorescence emission spectra of BSA (1 μM) is quenched in response to exposure to increasing concentrations of RB (from 0 – 9.4 μM). Note that fluorescence intensities have been corrected for dilution and inner filter effects. (B) Double log Stern-Volmer plots of RB quenching effects on BSA fluorescence measured at λ=338 nm. For RB-BSA complexes, the binding affinity estimated from the reciprocal intercept is K_d = 12.2 ± 1.1 μM and stoichiometry estimated from the slope is n = 0.65 ± 0.04, where ± represent 95% confidence intervals to the fitter parameter.

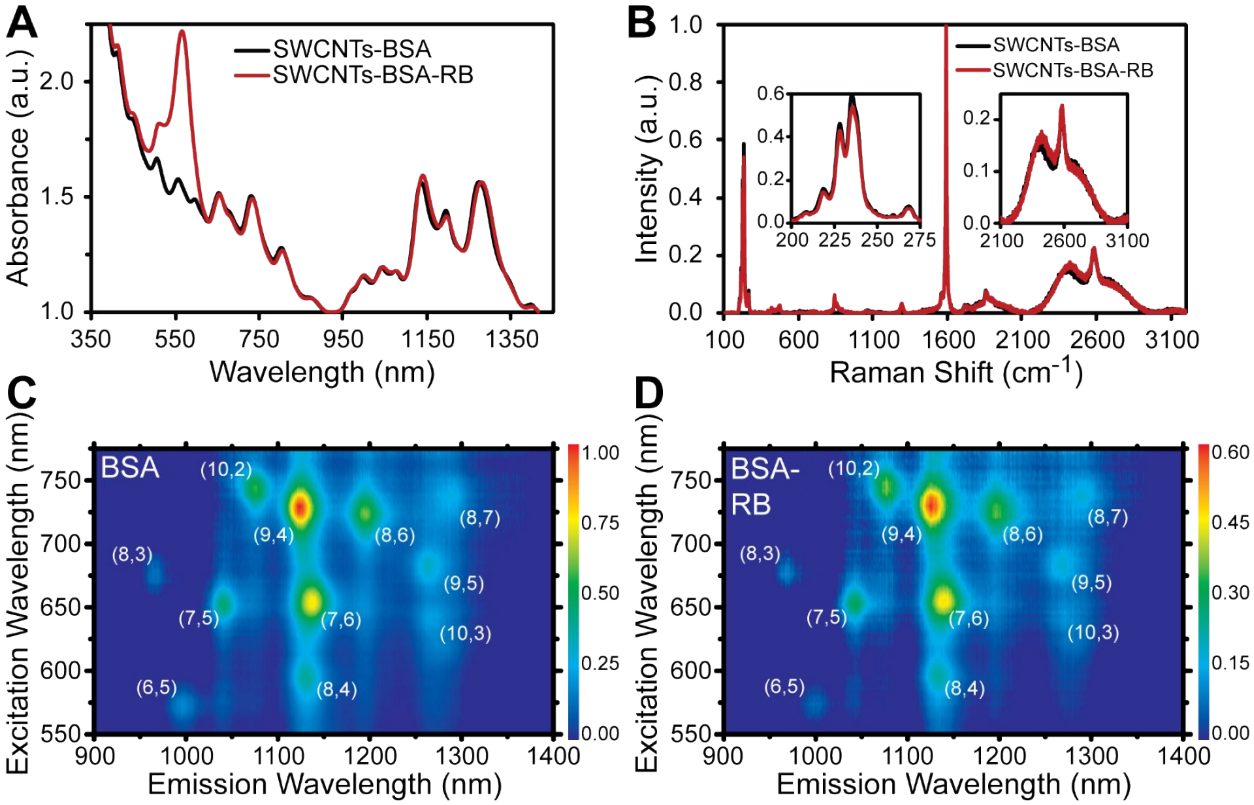

Fig. S4. Optical characterization of SWCNTs ternary complex dispersion with BSA and BSA-RB. (A) UV-vis-NIR absorbance spectroscopy of SWCNTs-BSA and SWCNTs-BSA-RB. The sharp peaks arise from the van Hove singularities of the density of states indicating individually dispersed SWCNTs. For SWCNTs-BSA-RB, the intense absorbance peak at ~550 nm results from RB loaded onto SWCNTs after removal of free RB through ultracentrifugation, washing, and re-dispersion in water. (B) Raman spectroscopy of SWCNTs-BSA and SWCNTs-BSA-RB confirms the dispersions maintain SWCNT structure with low I_D:I_G ratio and result in minimal aggregation with NIR fluorescence. The insets magnify the radial breathing modes (200-275 cm^{-1}) and the broad peak (~2100-3100 cm^{-1}) resulting from unfiltered real-space SWCNT fluorescence. (C-D) NIR fluorescence spectroscopy heat maps show SWCNT fluorescence intensity confirming the presence of individual SWCNTs for both SWCNTs-BSA and SWCNTs-BSA-RB with a similar distribution of chiralities. The dynamic range in both maps is scaled to the maximum NIR fluoresce intensity for SWCNTs-BSA.

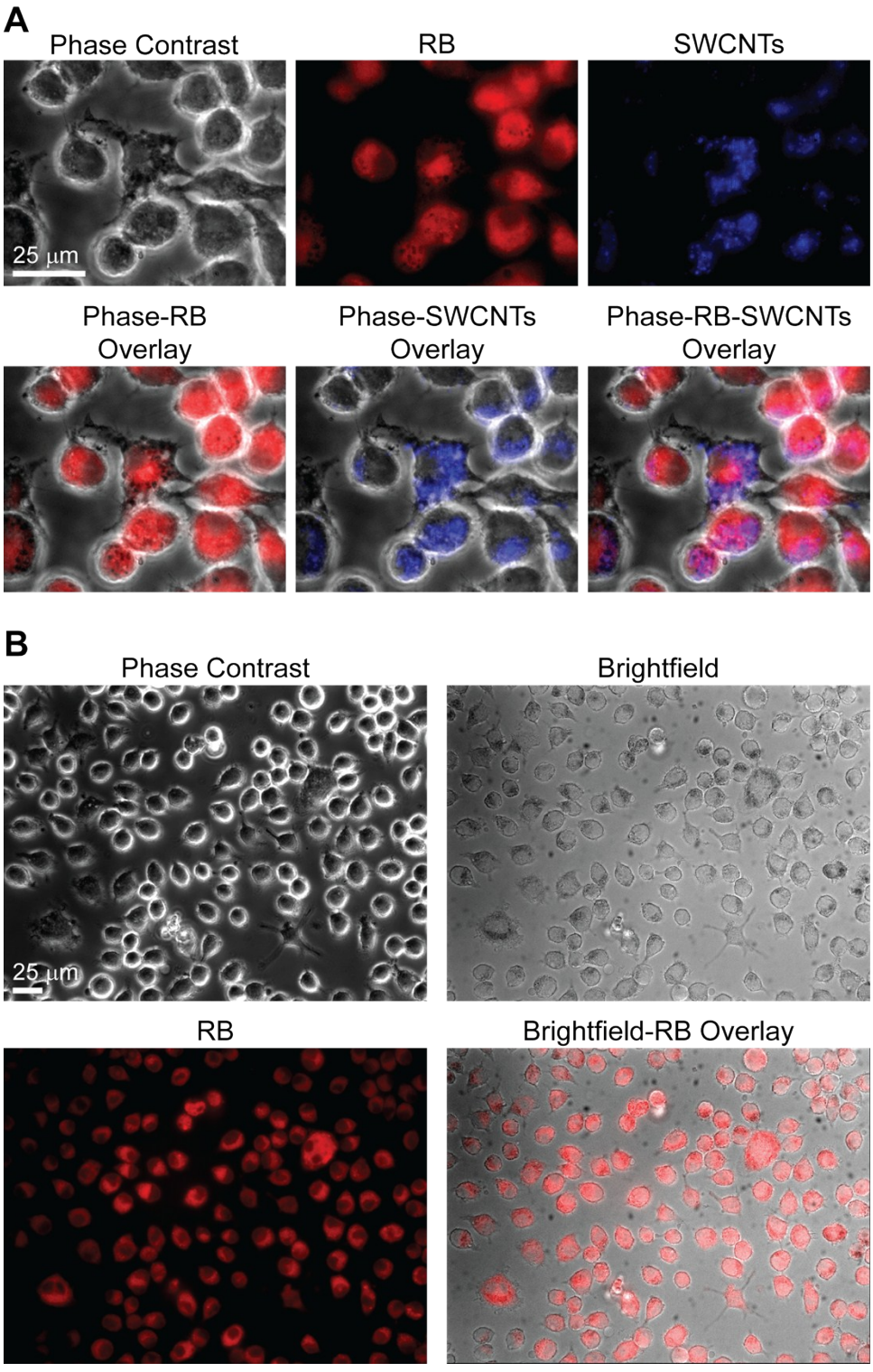

Fig. S5. Widefield fluorescence imaging of RB and SWCNT localization with transillumination overlays in macrophages exposed to 10 μg/mL SWCNTs-BSA-RB for 48 h. (A) High magnification imaging overlays of RB and SWCNT fluorescence with phase contrast illumination shows SWCNT intensity in phase dense subcellular regions within close proximity to spatially separate regions of increased RB intensity. (B) Low magnification imaging overlay of RB fluorescence with brightfield illumination in macrophages. Cells with increased contrast due to the absorbance of internalized SWCNTs also show increased RB fluorescence intensity.

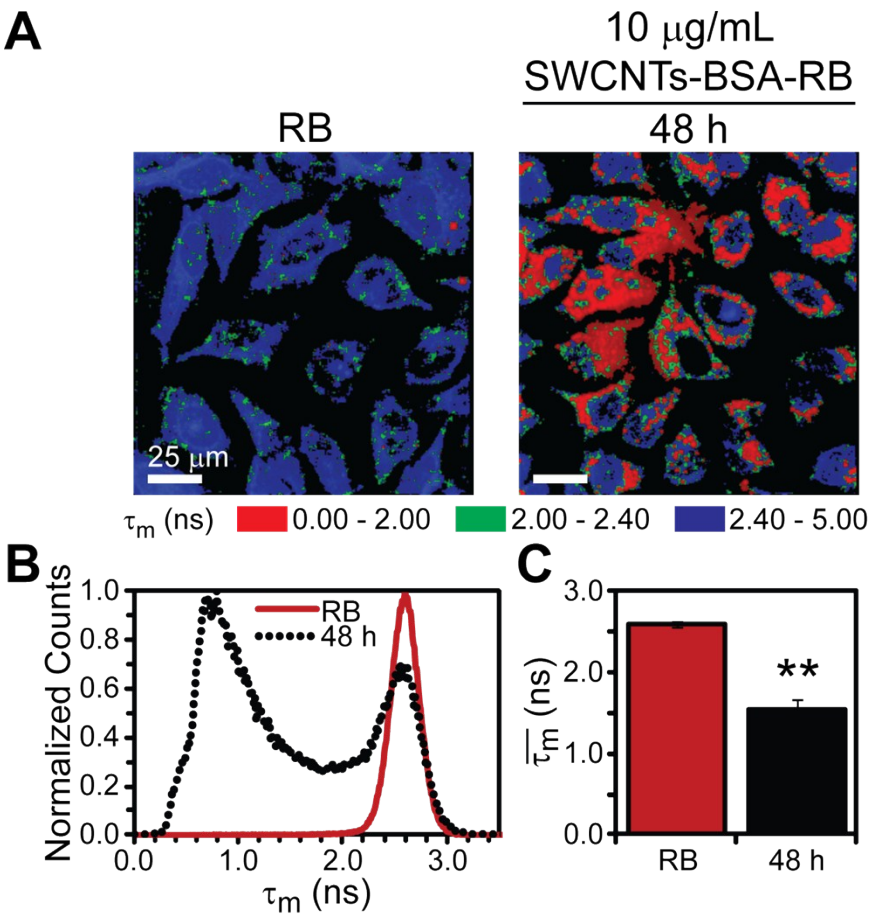

Fig. S6. FLIM of RB in HeLa cells exposed to 10 μg/mL SWCNTs-BSA-RB over 48 h. (A) Color coded mean fluorescence lifetime (τ_m) images. After 48 h of SWCNTs-BSA-RB exposure, HeLa cells show a heterogeneous distribution of quenched τ_m through the cytoplasm compared with cells exposed to equal concentrations of RB without SWCNTs. Note that each pixel represents a unique data point of τ_m. (B) Histograms of RB τ_m for all cells normalized to the maximum of each condition show that τ_m remains bimodal for HeLa cells, suggesting only partial release of RB from ternary complexes. (C) Quantitative comparison of the average τ_m for HeLa cells exposed to SWCNTs-BSA-RB remains significantly quenched after 48 h. Data = mean ± SEM, n ≥ 5 fields of view. Asterisks indicate statistical significance with **p<0.0001 compared to RB.

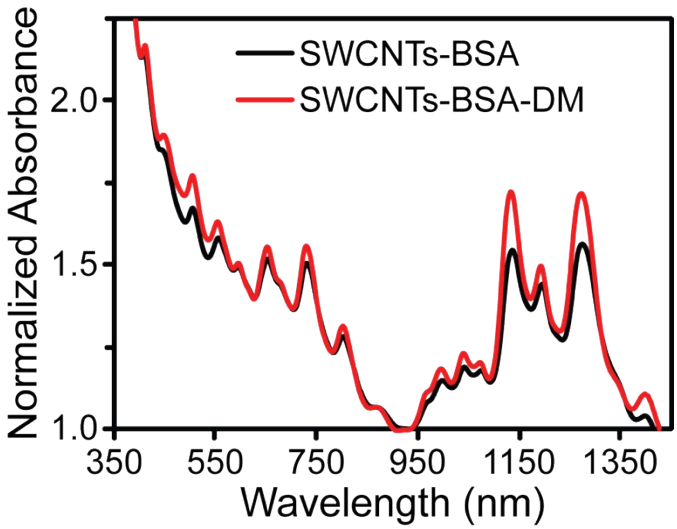

Fig. S7. UV-vis-NIR absorbance spectroscopy of SWCNTs-BSA-DM. The subtle increase in absorbance at ~485 nm results from DM loaded onto SWCNTs after removal of free DM and BSA-DM through ultracentrifugation, washing, and re-dispersion in water.

Supplementary References

1. D. Duhovny, R. Nussinov and H. Wolfson, in *Algorithms in Bioinformatics*, eds. R. Guigó and D. Gusfield, Springer Berlin Heidelberg, 2002, vol. 2452, ch. 14, pp. 185-200.
2. D. Schneidman-Duhovny, Y. Inbar, R. Nussinov and H. J. Wolfson, *Nucleic Acids Research*, 2005, **33**, W363-W367.
3. N. Andrusier, R. Nussinov and H. J. Wolfson, *Proteins: Structure, Function, and Bioinformatics*, 2007, **69**, 139-159.
4. E. Mashiach, D. Schneidman-Duhovny, N. Andrusier, R. Nussinov and H. J. Wolfson, *Nucleic Acids Research*, 2008, **36**, W229-W232.
5. J. C. Phillips, R. Braun, W. Wang, J. Gumbart, E. Tajkhorshid, E. Villa, C. Chipot, R. D. Skeel, L. Kalé and K. Schulten, *Journal of Computational Chemistry*, 2005, **26**, 1781-1802.
6. A. D. MacKerell, N. Banavali and N. Foloppe, *Biopolymers*, 2000, **56**, 257-265.
7. Y.-F. Xing, C.-F. Yang, Y.-F. Mo, M.-S. Wang and X.-G. Ma, *Journal of Materials Chemistry B*, 2014, **2**, 859-867.
8. S. Nosé, *The Journal of Chemical Physics*, 1984, **81**, 511-519.
9. W. Humphrey, A. Dalke and K. Schulten, *Journal of Molecular Graphics*, 1996, **14**, 33-38.
10. J. R. Lakowicz, *Principles of fluorescence spectroscopy*, Springer, New York, 3rd edn., 2006.
11. D. Agudelo, P. Bourassa, J. Bruneau, G. Berube, E. Asselin and H. A. Tajmir-Riahi, *PloS One*, 2012, **7**, e43814.
12. M. F. Islam, D. E. Milkie, O. N. Torrens, A. G. Yodh and J. M. Kikkawa, *Physical Review B*, 2005, **71**, 201401(R).
13. D. E. Johnston, M. F. Islam, A. G. Yodh and A. T. Johnson, *Nature Materials*, 2005, **4**, 589-592.
14. M. F. Islam, E. Rojas, D. M. Bergey, A. T. Johnson and A. G. Yodh, *Nano Letters*, 2003, **3**, 269-273.
15. M. S. Arnold, A. A. Green, J. F. Hulvat, S. I. Stupp and M. C. Hersam, *Nature Nanotechnology*, 2006, **1**, 60-65.
16. J. A. Fagan, M. L. Becker, J. Chun and E. K. Hobbie, *Advanced Materials*, 2008, **20**, 1609-1613.
17. M. L. Becker, J. A. Fagan, N. D. Gallant, B. J. Bauer, V. Bajpai, E. K. Hobbie, S. H. Lacerda, K. B. Migler and J. P. Jakupciak, *Advanced Materials*, 2007, **19**, 939-945.
18. B. D. Holt, K. N. Dahl and M. F. Islam, *Small*, 2011, **7**, 2348-2355.
19. B. D. Holt, K. N. Dahl and M. F. Islam, *ACS Nano*, 2012, **6**, 3481-3490.
20. B. D. Holt, M. C. McCorry, P. D. Boyer, K. N. Dahl and M. F. Islam, *Nanoscale*, 2012, **4**, 7425-7434.
21. P. D. Boyer, B. D. Holt, M. F. Islam and K. N. Dahl, *Soft Matter*, 2013, **9**, 758-764.
22. Y. Y. Huang, T. P. J. Knowles and E. M. Terentjev, *Advanced Materials*, 2009, **21**, 3945-3948.
23. M. J. O'Connell, S. M. Bachilo, C. B. Huffman, V. C. Moore, M. S. Strano, E. H. Haroz, K. L. Rialon, P. J. Boul, W. H. Noon, C. Kittrell, J. Ma, R. H. Hauge, R. B. Weisman and R. E. Smalley, *Science*, 2002, **297**, 593-596.
24. B. D. Holt, K. N. Dahl and M. F. Islam, *Journal of Materials Chemistry B*, 2015, **3**, 6274-6284.
25. P. Yaron, B. Holt, P. Short, M. Lösche, M. Islam and K. Dahl, *Journal of Nanobiotechnology*, 2011, **9**, 45.
26. B. D. Holt, H. Shams, T. A. Horst, S. Basu, A. D. Rape, Y.-L. Wang, G. K. Rohde, M. R. K. Mofrad, M. F. Islam and K. N. Dahl, *Journal of Functional Biomaterials*, 2012, **3**, 398-417.
27. R. R. Duncan, A. Bergmann, M. A. Cousin, D. K. Apps and M. J. Shipston, *Journal of Microscopy*, 2004, **215**, 1-12.
28. M. Köllner and J. Wolfrum, *Chemical Physics Letters*, 1992, **200**, 199-204.
29. W. Becker, *The bh TCSPC handbook*, Becker & Hickl GmbH, Berlin, Germany, 3rd edn., 2008.
30. M. S. Dresselhaus, G. Dresselhaus, R. Saito and A. Jorio, *Physics Reports*, 2005, **409**, 47-99.

31. D. A. Heller, P. W. Barone, J. P. Swanson, R. M. Mayrhofer and M. S. Strano, *Journal of Physical Chemistry B*, 2004, **108**, 6905-6909.
32. S. M. Bachilo, M. S. Strano, C. Kittrell, R. H. Hauge, R. E. Smalley and R. B. Weisman, *Science*, 2002, **298**, 2361-2366.
33. B. Koh, G. Kim, H. K. Yoon, J. B. Park, R. Kopelman and W. Cheng, *Langmuir*, 2012, **28**, 11676-11686.
34. A. Ahmad, T. Kurkina, K. Kern and K. Balasubramanian, *ChemPhysChem*, 2009, **10**, 2251-2255.
35. S. M. Tabakman, K. Welsher, G. Hong and H. Dai, *Journal of Physical Chemistry C*, 2010, **114**, 19569-19575.
36. R. F. Kubin and A. N. Fletcher, *Journal of Luminescence*, 1982, **27**, 455-462.